
Article:
Zubairi, H. orcid.org/0000-0002-5332-3554, Hussain, F., Sheikh, S. et al. (3 more authors) (2023) Comparative study of cold assisted and conventional sintering of (1-2x) K0.5Na0.5NbO3-xBaTiO3-xBiFeO3 multiferroic ceramics. Materials Science and Engineering: B, 296. 116632. ISSN 0921-5107

https://doi.org/10.1016/j.mseb.2023.116632

Comparative Study of Cold Assisted and Conventional Sintering of (1-2x) $K_{0.5}Na_{0.5}NbO_3$-x$BaTiO_3$-x$BiFeO_3$ Multiferroic Ceramics

Hareem Zubairi[1*], Fayaz Hussain[1], Sajida Sheikh[1], Asif Ahmed Shaikh[1], Dawei Wang[2] and Ian M Reaney[3*]

[1] Department of Materials Engineering, NED University of Engineering and Technology, 75270, Karachi, Pakistan; fhussain@neduet.edu.pk (F.H.); sajidasheikh02@gmail.com (S.S.); asif.shaikh@neduet.edu.pk (A.S)

[2] wangdawei102@gmail.com (D.W.)

[3] Department of Materials Science and Engineering, The University of Sheffield, UK,

* Correspondence: zubairihareem@gmail.com (H.Z.); i.m.reaney@sheffield.ac.uk (IMR)

Abstract: (1-2x) $K_{0.5}Na_{0.5}NbO_3$-x$BaTiO_3$-x$BiFeO_3$ (KNN-BTO-BFO) lead-free ceramics fabricated by Conventional Sintering (ConS) and Cold Assisted Sintering (CAS) were studied using X-ray diffraction, scanning electron microscopy and their dielectric, piezoelectric and magnetic properties characterised. Orthorhombic KNN transformed to tetragonal for compositions with $x \geq 0.03$ for ConS and CAS. The relative density attained for CAS (1080-1100ºC) samples was consistently higher than ConS (1140-1180ºC) for equivalent compositions, despite the lower sintering temperature. The higher relative density in CAS with respect to ConS samples is attributed to the higher ('super') green density achieved through cold sintering in comparison with dry pressing. The permittivity maxima for undoped KNN occurred at 420°C and 400°C, respectively, for CAS and ConS samples with ConS samples exhibiting a broader permittivity maximum at the orthorhombic to tetragonal transition and higher dielectric loss, particularly above 190°C. The permittivity maxima decreased in temperature and broadened as a function of x in each case. For x = 0.01, the piezoelectric coefficient was maximum (d_{33} = 125 pC/N) for CAS with coupling coefficient, k_p = 0.3. A magnetization of 0.09 emu/gm was obtained for CAS at x = 0.05, with only 0.06 emu/gm for ConS, likely due to the lower density for the latter sintering method. These preliminary results demonstrate that KNN-based ceramics may be densified using CAS at temperatures lower than conventional whilst still retaining promising values of permittivity, piezoelectric coefficient, and magnetization.

Keywords: cold sintering; conventional sintering; dielectric properties; magnetization

1. Introduction

Due to their exceptional dielectric properties, large piezoelectric coefficients and high Curie temperature (T_c), $K_{0.5}Na_{0.5}NbO_3$ (KNN)-based lead-free ceramics are considered the most probable substitute for lead zirconate titanate (PZT) [1–7]. However, KNN-based compositions are notoriously difficult to densify using Conventional Sintering (ConS) and the reproducibility of dielectric and piezoelectric properties suffers as a result [8]. Ideally, a reproducible method of achieving high relative density is required which also permits substitution by the appropriate dopants to optimize properties [3]. The challenge, now, is to produce high-quality, sustainable, and environmentally friendly ceramics products. As a result, various sintering methods were developed to reduce temperature, time, energy, and cost of preparation to produce good quality products as compared to conventional sintering methods that have been in use for centuries [9–11]. The strategies embraced adopted the methods that may add liquid to modify the arrangements of particles and promotes diffusion and bond-making at low temperatures, shrinking the particle size, use of external pressure like sinter forging, hot isostatic pressing, hot pressing, etc., and the use of externally applied energy. Hence, several authors have pursued low temperature/energy densification KNN ceramics to improve density and achieve a more sustainable method of production [2,12–18] such as flash sintering, spark plasma sintering, microwave-assisted sintering, etc [11,17,19–23].

Densification of KNN has been reported at <200°C through a cold sintering process (CSP) in which dissolution-precipitation is activated [12,17,24–29] through the application of uniaxial pressure in the presence of a transient (aqueous) solvent [30,31]. In this procedure, particles that have sharp edges and points are broken down, reducing interfacial areas, which helps to consolidate and reorganize the particles of the ceramics. The liquid phase redistributes itself, filling the spaces between particles with the help of external and capillary pressures [30]. The "dissolution-precipitation" process, which occurs when water evaporation causes the liquid phase to reach a supersaturated condition over 100ºC [32], generates enormous forces that provide the surface area to the chemical (solid and liquid) to attain high levels of densification. Dissolution then causes the liquid to become supersaturated [31] followed by densification as the water evaporates and precipitation

occurs [32]. To facilitate the arranging process and create appropriate interfaces for dissolving the various particles, it requires an external pressure of between 50 and 500MPa. The composition of the aqueous phase can change, and it can contain species that are known to form organic salts with the host material, such as acetic acid. Such approaches have been used in the cold sintering of compounds such as $BaTiO_3$, ZnO and CeO_2 [2,8,33]. CSP has been used to produce more than 70 inorganic materials up to this point [30,34–36]. In addition to most dissolved compounds (congruently), which can be directly subjected to cold sintering like $K_2Mo_2O_2$ and NaCl, some of the incongruent compounds require the assister-or-post annealing procedures to achieve high densification in the resultant compounds like $BaTiO_3$, $Na_{0.5}Bi_{0.5}TiO_3$, PZT, and others [37–39]. To this time, research published in scientific journals has demonstrated that the CSP can manufacture densified ceramic compounds of more than 50 different compositions at temperatures below 300 °C, with a density gain of between 80~99% (theoretically). However, many compounds cannot be processed and densified using CSP because they require higher temperature ranges to make bonds. As a result, these compounds have been assisted sintered at a temperature that is significantly lower than the average temperature for conventional sintering. For example, zirconia ceramics are normally sintered at 1400°C; however, when they were treated to CSP, they were assisted sintered at 1200 °C. This was possible because of congruent dissolution and minimal segregation throughout the precipitation process. Although, the incongruent dissolving behaviour of $BaTiO_3$ (BTO) [40–42] has been investigated and when they are subjected to CSP at 180 °C later on subjected to assister heat treatment, so they produced ~95% denser samples with the carbonate-rich glass phase, similarly for $BiFeO_3$ (BFO) [43] in the presence of alkaline transient fluxes [13]. So, the incongruent and congruent dissolutions are involved, and the cold-assisted sintering can be easily used to improvise the green density of the ceramics by reducing the temperature to the great extent.

The major step for the "dissolving precipitation" procedure is using the water at low temperatures to provide congruent dissolution while increasing the density of the ceramic. Unfortunately, incongruent dissolution is common in many multi-component materials, many of which also have low water solubility, particularly in configurations where atoms/molecules/ligands are tightly packed

together and have strong chemical interactions between them [44]. Although, during CSP, the samples became exceedingly brittle, and they are difficult to handle without assisted heating/sintering. As KNN doesn't support the bond formation at low temperatures, it will break when subjected to drying, when prepared at room temperature. So, to hold the particles together and improvise their linking, the KNN has been doped and the amorphous precipitates having de-ionized water made bond together at CSP ranges, to increase the density and strength of the samples [32]. The highest relative density of sintered ceramics reaches 98% when the water content is raised to 10 wt.%. This is on par with the relative densities reached by utilising pressure-assisted sintering processes such as spark plasma sintering and hot press sintering. When the percentage of water reaches 15% by weight, the green and sintered densities will both see a small decrease. Sintering density would reduce as a consequence of the green density decreasing as a result of the increase in pore volume induced by the loss of excessive water generated by evaporation [45]. For example, deionized water was used to create a potassium-rich phase in the cold sintered KNN ceramics as the liquid medium, and this helped to limit the volatilization of alkali metal components, which in turn helped to improve the electrical characteristics of KNN [46]. Therefore, the post or assisted sintering is needed to sinter the samples over 1000°C to provide densification at optimum, resulting in a divergence from the stoichiometric ratio owing to the volatilization of K_2O and Na_2O during annealing, resulting in a loss of density. Similarly, at an aqueous pH of 12, $BaTiO_3$ (BTO) is known to be thermodynamically unstable [47]. The BTO when subjected to water, Ba+ ions leached from the surface area, resulting in a Ti-rich and amorphous passivated layer. These active spots on the crystal surface are physically separated from the saturated solution by this amorphous layer. As a result, epitaxial growth provides a hindrance to crystal development in the supersaturated solution. The BTO ceramics could not be densified in our early trials using just a water solution, as is generally required for CSP. Moreover, it has been reported that bismuth ferrite composition, $BiFeO_3$, has been widely used in the electroceramic industry [43]. However, due to the high curie temperature, permanent magnet behaviour, and low cost, microwave, and electromagnetic shielding are being utilized. These magnetic and permeable materials usually resonate with relative permittivity, i.e., $\varepsilon_r \sim 25$ at low

values of frequency (~4.5kHz) but when done with the cold sintering, the densification and value of ε_r have been drastic increases by favouring the conductivity concerning the content of BFO in a material [43].

However, many systems, including KNN, exhibit incongruent dissolution in deionized water in which potassium leaches from the host phase to form an alkaline liquid medium [46]. Some obstacles remain in the development of KNN-based ceramics, such as bottlenecks in preparation technologies, imbalanced electrical property development, and gaps between ceramic characteristics and device requirements. Because potassium is very reactive, KNN-based ceramics absorb moisture rapidly throughout the preparation process [48]. Furthermore, the electrical properties of KNN-based ceramics are extremely sensitive to some technological parameters (for example, calcining temperature, sintering temperature, and poling process), and the volatility of potassium and sodium during the preparation process results in decreased densification. Therefore, the challenges that KNN faces in replacing PZT in most applications are linked to limitations in KNN production and sintering. In KNN, the number of successful attempts that achieved above 95% density is quite restricted. The main issues are related to KNN's poor sintering performance due to a restricted range of sintering temperatures, alkali element volatilization, and secondary phase development. According to the phase diagram of $KNbO_3$- $NaNbO_3$, the solidus line lies at 1140ºC [49,50]. The KNN system possesses phase stability up to 1140ºC, which is a low temperature for reaching full density; above this temperature, alkaline evaporation takes over. According to recent research, evaporation is crucial after 950°C. However, to date, there are no reports of promising piezoelectric properties for KNN except where ceramics have undergone post-cold-sintering heat treatment (referred to here as Cold-Assisted Sintering (CAS) and even fewer have attempted to optimize doped compositions which have the potential to compete commercially with PZT.

The rationale of this work is to compare the microstructure, structure, densification and physical properties of $(1\text{-}2x)K_{0.5}Na_{0.5}NbO_3$-$xBaTiO_3$-$xBiFeO_3$ (KNN-xBFO-xBTO) ceramics prepared by CAS and ConS [12,24]. Substitution of BTO [4,8,51] and BFO [5] have been shown to promote

structural changes in KNN ceramics that result in the optimisation of piezoelectric properties but to date, such compositions have not been evaluated using CAS.

2. Materials and Methods

Na_2CO_3 (>99.8%, Sigma Aldrich), K_2CO_3 (>99%, Sigma Aldrich), Nb_2O_5 (>99.99%, Sigma Aldrich), Bi_2O_3 (>99.9%, Sigma Aldrich), Ba_2CO_3 (>99.0% Sigma Aldrich), Fe_2O_3 (>99%, Sigma Aldrich), and TiO_2 (>99.0% Sigma Aldrich) were preheated and weighed to give the appropriate ratios in the solid solution, (1-2x) $K_{0.5}Na_{0.5}NbO_3$-x$BaTiO_3$-x$BiFeO_3$ ((1-2x)KNN-xBFO-xBTO) with x = 0.00, 0.01, 0.03, and 0.05. The preheated batches were mixed/milled for 2 h in a planetary ball mill in ethanol to achieve D_{50} ~5.1 µm. To remove the ceramic from its volatile impurities, the particles that had been mixed were first dried and then calcined for four hours at 850°C with a heating and cooling rate of 10 °C/min. To obtain a substance that was uniformly mixed, the post-ball milling/mixing was carried out again in a planetary ball mill for a total of two hours. The powders that were produced were then sieved before being milled or mixed again with a mortar and pestle together with a small quantity of deionized water [45], and 6wt% Polyvinyl Alcohol (PVA) [52] for conventional sintering. For the process of cold sintering, the wet powder (prepared with deionized water at a volumetric concentration of 30 vol%) was placed in a die with a diameter of 12.7 mm and a heater connected that could reach temperatures of up to 500°C. The cold sintering process is the basis of exerting a pressure of 350–360 MPa while maintaining a temperature of 120–150°C for a period of 30 minutes. After the samples that had been cold sintered had been heated for a further 4 hours at 120°C to eliminate any remaining moisture, they were again sintered for 4-5 hours at temperatures ranging from 1080 to 1100 °C. In the conventional sintering process, samples were first heat treated at 600°C to remove the PVA binder, and then they were sintered for two hours at temperatures between 1140~1180°C.

A Laser Particle Analyser (Model no. BT-9300H) was utilized to determine particle size operated at 220 V, 50/60 Hz, and 100W with agitator speed 500-2500 rpm having a size range of 0.1µm to 340µm and test time 1-3 minutes. The light source in the analyzer is a semiconductor laser

diode having a wavelength of 635nm with a power of 3mw. After sintering, density was measured with the Archimedes method using water as the immersion liquid (densities were also measured using a geometric method). The identification of phases and chemical composition was evaluated by the XRD (PANalytical, X'Pert Pro, made in the Netherlands) at room temperature. The XRD was operated at 220V, 50/60 Hz, and 8.5KVA with a scanning rate of 0.02/min with the scan step size 0.6s between the angles 10 to 80 degrees (2□) with a step size of 0.025 2□ and scanning time of 0.6000s using Cu Kα radiation. The XRD results were analysed by HighScore Plus using PDF-4+ (2022) through Rietveld Analysis. Crystal structures were generated using Highscore Plus files from CrystalMaker software version 10.7.1. A Scanning Electron Microscope (SEM, JEOL JSM 6380L) operating at 5.0 kV was used to image the microstructure of samples.

An Inductance, Capacitance, and Resistance meter (LCR, TH2826 Changzhou Tonghui Electronic Co., Ltd., Changzhou, China) was used to measure dielectric properties as a function of frequency and temperature operated at 110V/60Hz – 80VA and 220V/50Hz – 80VA. Poling of samples was carried out at 27°C using a high voltage DC power supply (4 kV for 10 minutes, where the thickness of all samples was 1.50 mm respectively) with the sample suspended in silicone oil. Piezoelectric coefficients (d_{33}) were recorded after poling by using a SINOCERA meter (YE2730A d_{33} Meter) and the electromechanical coupling factor (k_p) was calculated from a resonant method using an LCR/impedance meter (TH2826 Changzhou Tonghui). A Vibrating Sample Magnetometer (VSM) by MicroSense (Model No. 1660 MRS) was made in the USA and used at 32V and 0.07A with a maximum output of 130V and 75 A (DC) to measure the Magnetisation (M) versus Magnetic Field (H) hysteresis loops to confirm the appearance of magnetic properties in these ceramics.

3. Results and Discussion

Figure 1(a) depicts the green and as-cold sintered densities and figure 1(b) shows the sintered relative densities of ConS and CAS samples as a function of x, based on data shown in Table 1. All CAS have a higher relative density compared to ConS samples of equivalent composition [32] The theoretical density of each composition is calculated by using the CrystalMaker, using the data

evaluated through Rietveld Analysis, from the unit cell volume and mass of the ions. However, for both sets of samples, the evolution of density is non-linear with the maximum in each case achieved for x=0.01. When compared to samples made using the standard dry pressing procedure, cold sintered samples have a greater degree of green density, sometimes known as a "super-green" condition. The super-green bodies that are produced by cold sintering allow for a sintering process that is both more effective and quicker when it is post-heat treated. This is because they have higher relative densities (around 95.8%) that can be achieved at lower temperatures than conventional samples (around 91.8%). When the densification was increased using the cold sintering process, similar trends were also reached in the earlier study, and when assisted sintered, it drastically increases [8,15,36,45]. This happens because cold sintering is performed at a greater pressure, and on the application of higher pressure, the transient fluid, deionized water, diffuses the ceramic particles into one another properly and forms the interlinked bonding. As a result, this phenomenon is observed [53]. Furthermore, when the samples are taken to assisted sintering, the diffusion phenomenon proceeds abruptly and the sampling gain has a higher density, which is also shown in this study.

Table 1. Density Measurements

Process	Composition	Green Density (g/cm^3)	Theoretical Density (g/cm^3)	Bulk Density (g/cm^3)	Relative density (%)
CAS	x=0.00	3.2201	4.5875	4.3331	94.129
	x=0.01	3.2039	4.6889	4.5017	95.852
	x=0.03	3.3829	4.7632	4.4149	92.111
	x=0.05	3.5254	4.9419	4.3682	86.866
ConS	x=0.00	3.0939	4.5875	3.5221	69.751
	x=0.01	3.0726	4.6889	4.3337	91.804
	x=0.03	3.1228	4.7632	4.1071	84.025
	x=0.05	3.2360	4.9419	4.0241	77.192

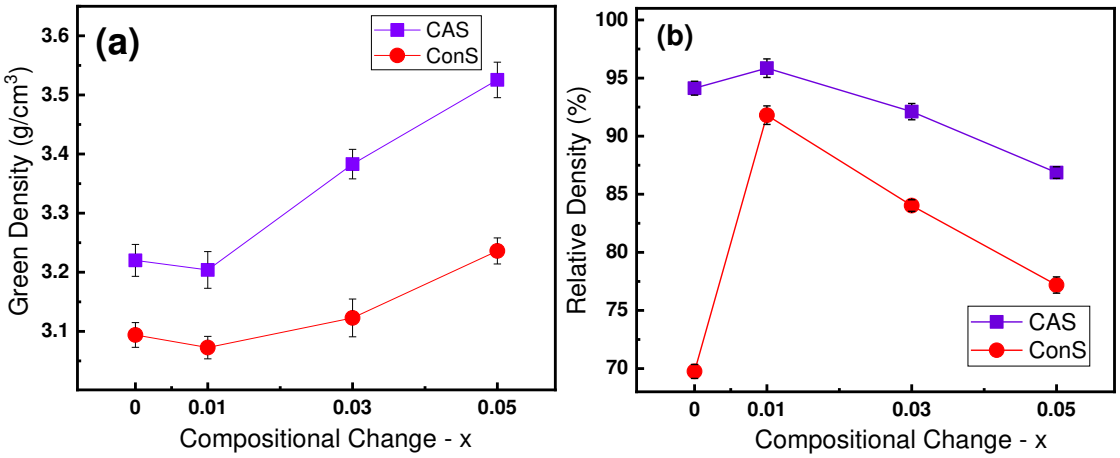

Figure 1. Comparison of densities of (1-2x) KNN – xBFO – xBTO (a) green and as-cold sintered samples (b) sintered samples as a function of x.

The XRD patterns of KNN-xBFO-xBTO ceramics that were fabricated by CAS are shown in Figure 2a. It has been determined that all of the diffraction peaks belong to a single perovskite phase, which suggests that BTO and BFO combine to form a solid solution. The incorporation of the BFO compound with a volume of 125.72 $Å^3$[54] and BTO with a unit cell volume of 64.41$Å^3$[55] having a tetragonal structure into the KNN matrix compound may result in a decrement of the overall volume[56] of the composition in the study, which causes the diffraction peaks to move to higher angles as x increases. This decrease in cell volume is responsible for the shift. The diffraction peaks at 45° (2θ) are highlighted in Figure 2b, which also illustrates the change in a peak form can alter depending on the value of x. As can be seen in Figures 2 and 3, the shift from a triplet peak to a doublet peak indicates that the RT composition has shifted from an orthorhombic phase to a tetragonal phase for $x \geq 0.03$, in the case of CAS and ConS [57–60]. The transformation sequence is shown to be valid as a function of x in Table 2, which displays the space groups that were refined based on the XRD data using the Rietveld analysis.

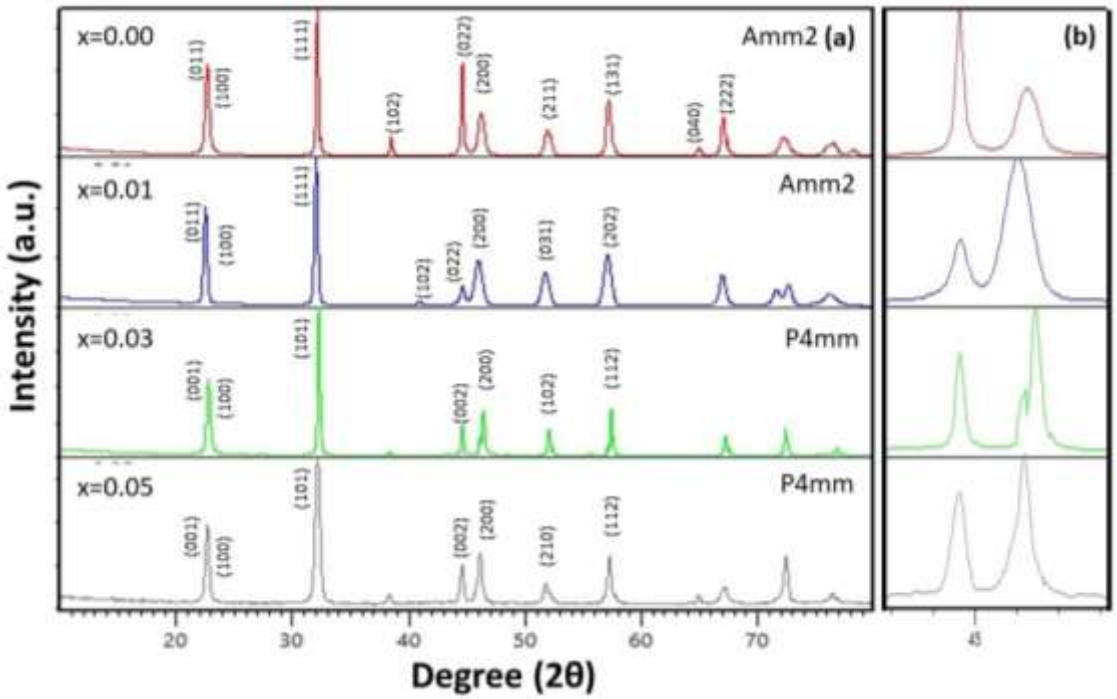

Figure 2. (a) XRD of sintered compositions of (1-2x) KNN-xBFO-xBTO by CAS (b) enlarged 45° peak

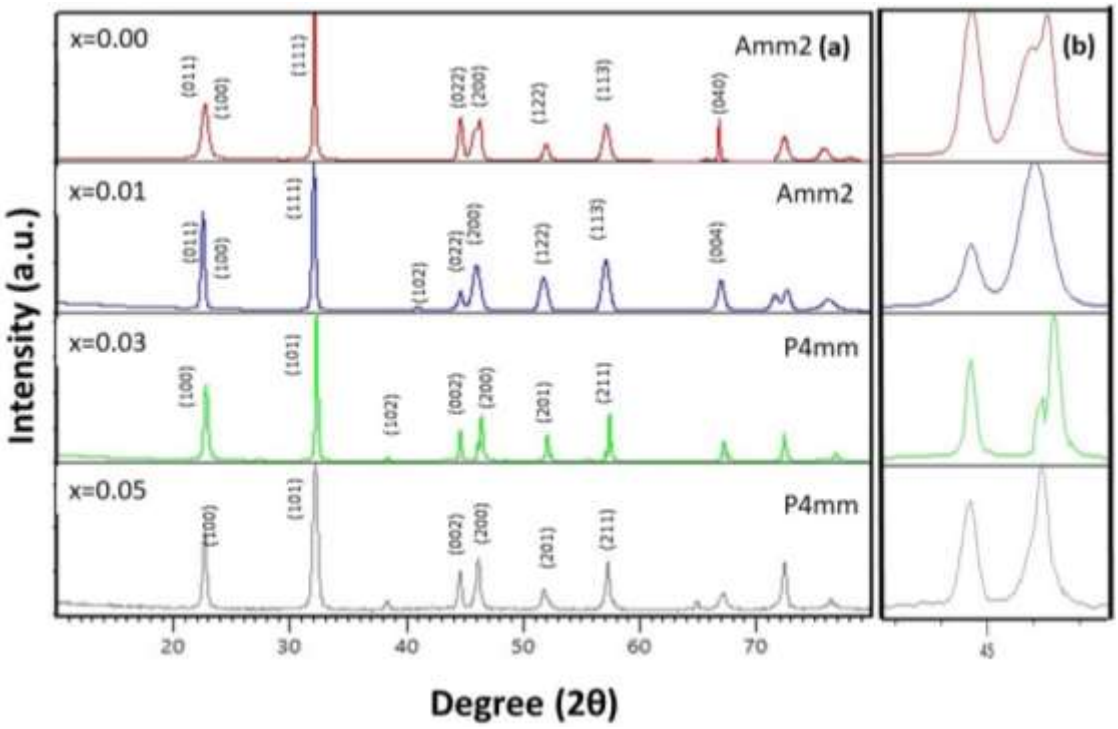

Figure 3. (a) XRD of sintered compositions of (1-2x) KNN-xBFO-xBTO via ConS (b) enlarged 45° peak

Table 2. Refined space groups and crystal classes as a function of x for both sintering methods (CAS & ConS) through Rietveld Analysis.

Process	Composition	ICDD No. (used for Rietveld Analysis)	Crystal Structure	Lattice Parameters			The volume of the cell (Å^3)	Space Group
				a (Å)	b (Å)	c (Å)		
CAS/ ConS	x=0.00	01-085-7128	Orthorhombic	3.94 (1)	5.64 (3)	5.72 (1)	125.440(4)	Amm2
	x=0.01	04-025-8304	Orthorhombic	3.98 (2)	5.64 (1)	5.61 (3)	122.304(2)	Amm2
	x=0.03	04-016-8143	Tetragonal	4.14 (5)	4.14 (2)	4.17 (1)	71.272(5)	P4mm
	x=0.05	04-016-8143	Tetragonal	3.76 (1)	3.76 (1)	3.76 (3)	53.137(3)	P4mm

Figure 4 represents the SEM micrographs that were taken of the fracture surfaces of ceramics that were fabricated by CAS. The microstructure exhibits porosity in the structure. It has been observed that the amount of BFO and BTO in KNN ceramics have an obvious impact on the morphology. The cuboidal grain shape in the micrographs represents the typical KNN-based compositions, and the grain size decreases from 2.6 to 1.22µm as a function of x. The composition with x = 0.01 displays the least porosity, which is commensurate with the highest observed density, ~95% [17,55,61,62].

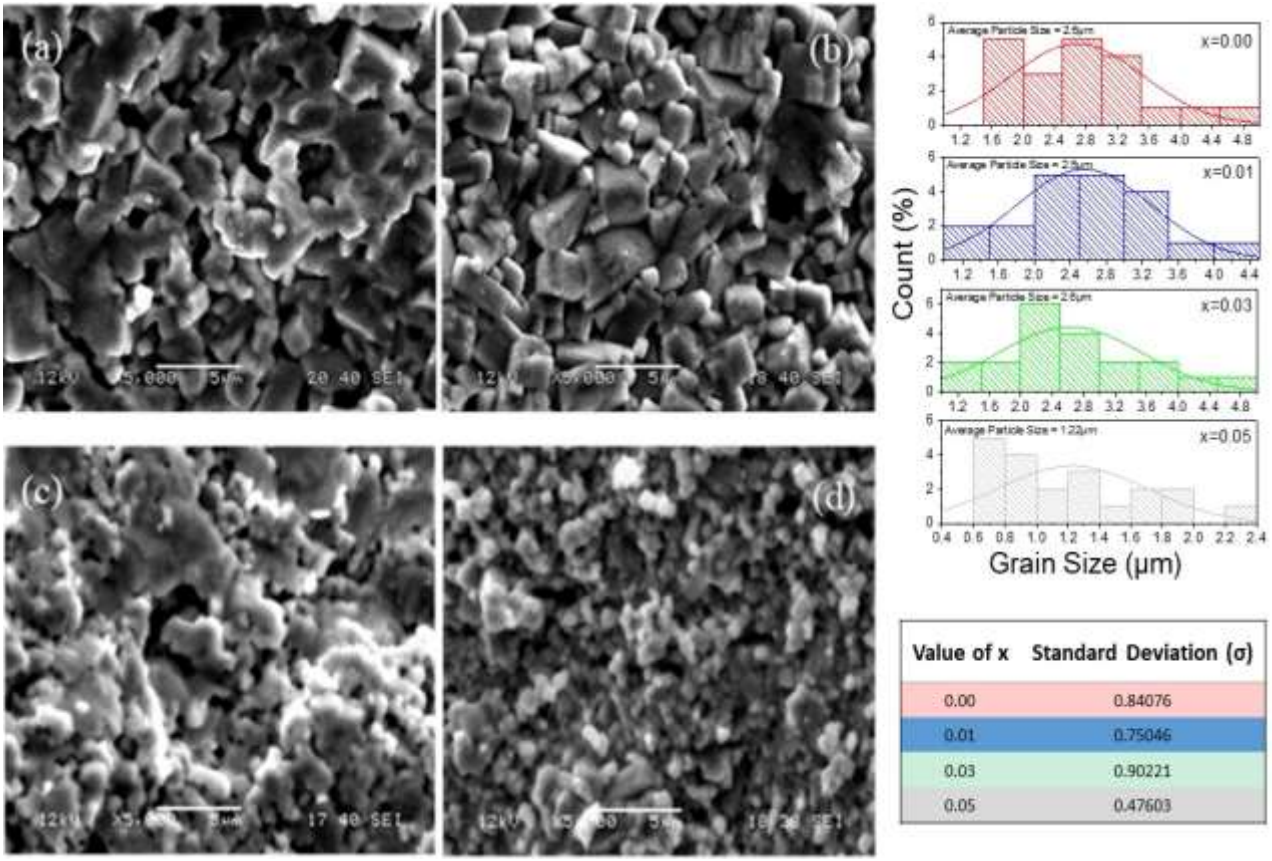

Value of x	Standard Deviation (σ)
0.00	0.84076
0.01	0.75046
0.03	0.90221
0.05	0.47603

Figure 4. SEM Micrographs with their grain size distribution and standard deviation values of KNN-xBFO-xBTO of CAS samples with (a) x=0.00 (b) x=0.01 (c) x=0.03 and (d) x=0.05

Figures 5a and b present the temperature dependence of relative permittivity (ε_r) and dielectric loss (tanδ) for all prepared ceramics. Not only is T_C higher for undoped CAS ceramics but the orthorhombic to tetragonal transition temperature ($T_{O\text{-}T}$, ≤ 211.4°C) is higher than in ConS (≤196.2°C) samples for x = 0.00 and x = 0.01, figures 5e and 5f [33,34,40,43,47,63,64]. Moreover, tanδ is also consistently lower in CAS with respect to ConS samples, Figure 5 (b) & (d) (Table1). We propose that the higher 'super green' density of CAS pellets with respect to the dry-pressed green density of ConS allows faster and greater densification at lower sintering temperatures. Thus, ConS samples have a higher concentration of A-site cation vacancies with respect to CAS samples which leads to a lowering of T_C and $T_{o\text{-}T}$ (evaluated from LCR data), as shown in Figures 5e & f, and a high tanδ due to contributions from space charge [9,11,31,34,49,65–69]. Moreover, the broadening of transitional peaks observed while additions of BTO and BFO, which indicates the transformation of non-linear to linear dielectric class of perovskite ceramics.

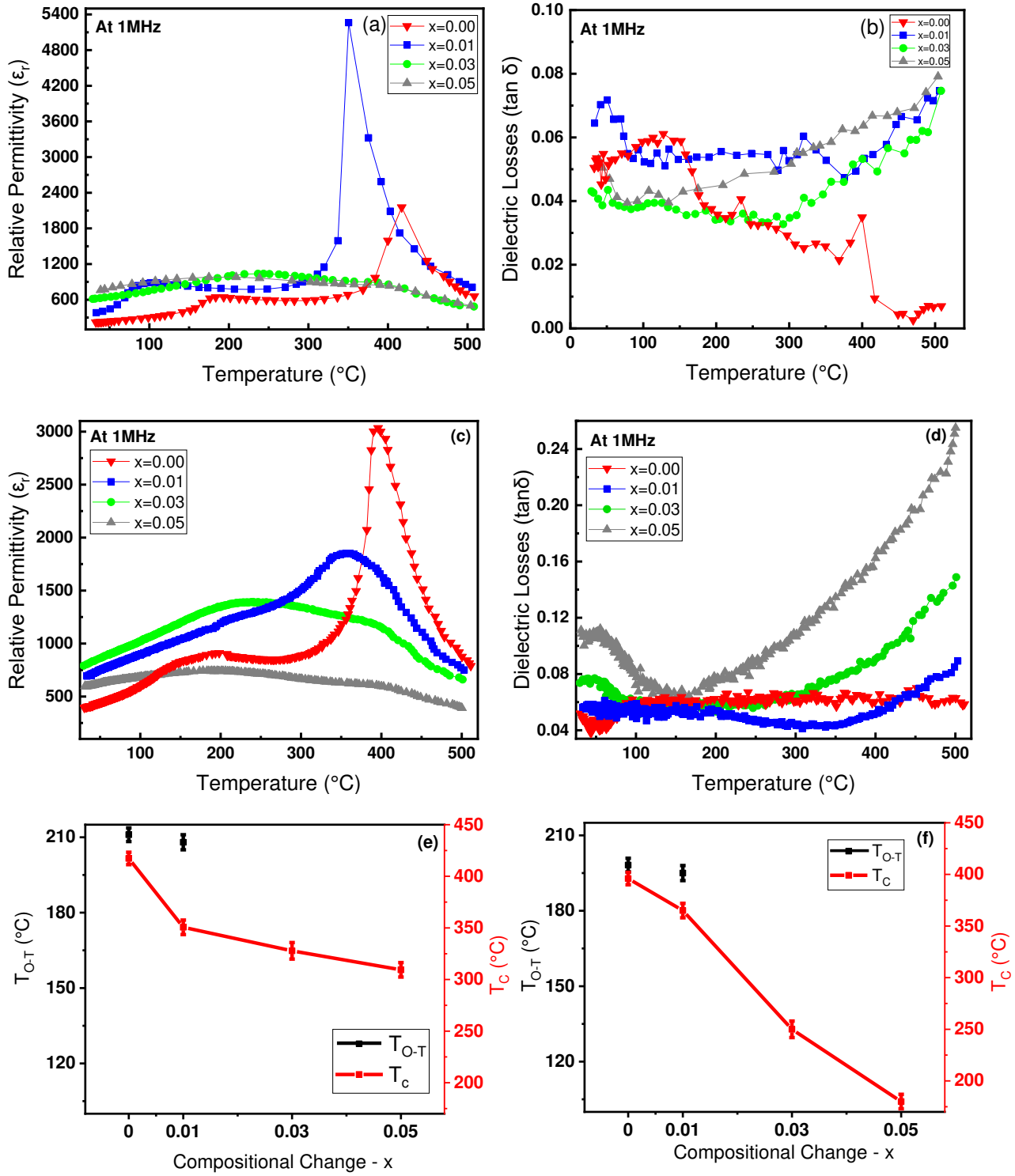

Figure 5. (a) The relative permittivity and (b) dielectric loss of KNN-xBFO-xBTO by CAS at 1MHz (c) Relative permittivity and (d) dielectric loss of KNN-xBFO-xBTO ConS ceramics at 1MHz. (e) T_{O-T} and T_C for CAS samples. (f) T_{O-T} and T_C for ConS samples

Figure 6 shows the d_{33} and k_p as a function of x for all prepared samples. Maximum d_{33} and k_p were obtained for x=0.01, 125.3 pC/N and 0.35 for CAS. ConS samples show a steady decrease in d_{33} and k_p with x, whereas CAS samples showed an increase in d_{33} until x = 0.01 but a steady decline thereafter. The low values of d_{33} and k_p are due to the low density of ConS samples but we note that even CAS samples do not show particularly high values despite their superior density. Further work is required to understand why d_{33} and k_p do not scale with density for cold sintering.

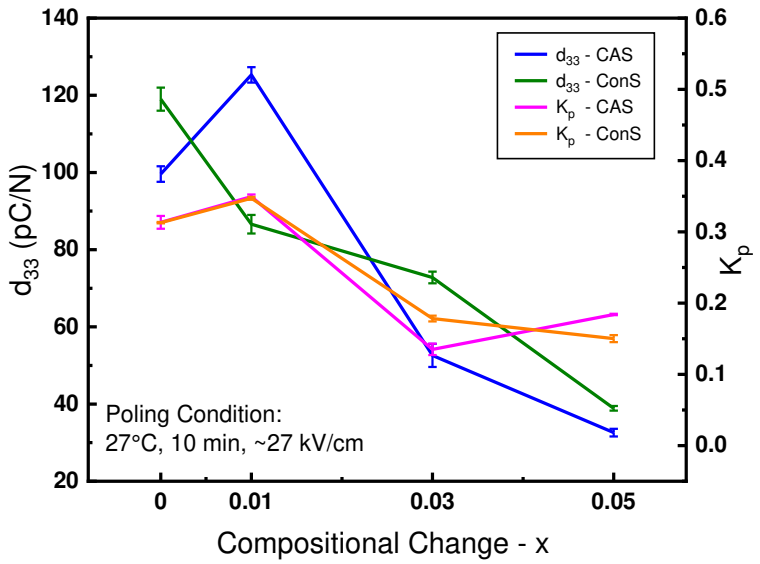

Figure 6. Piezoelectric coefficient (d_{33}) and electromechanical coupling factor (k_p) of KNN-xBFO-xBTO sintered by (a) CAS; (b) ConS.

Figure 7 displays the magnetization (M) vs. Magnetic Field (H) measurements of (1-2x) KNN-xBFO-xBTO ceramics at room temperature. The magnetic properties are saturated as the concentration of BFO and BTO was increased, indicating the addition of the dopant improvising the soft ferrimagnetic behaviour in the ceramics. The optimised magnetization (M_s) and remanent magnetization (M_r) values in each case of sintering processes were compared at x=0.05 (in the case of CAS: M_s = 0.095434 and M_r = 0.04 emu/gm, and in the case of ConS: M_s = 0.06 and M_r = 0.02 emu/gm) for low coercive fields. M_s and M_r are generally larger for CAS samples in comparison to ConS samples for the same value of x due to the higher density which enhances the degree of magnetic alignment between grains, ultimately resulting in greater hysteresis for x = 0.05 [70–73].

However, the weak ferrimagnetism in the $0.00 \leq x \geq 0.03$ relates to the presence of the magnetic interactions of less F^{3+} content from BFO by not compensating the configuration of magnetic spins in the ceramics [74,75].

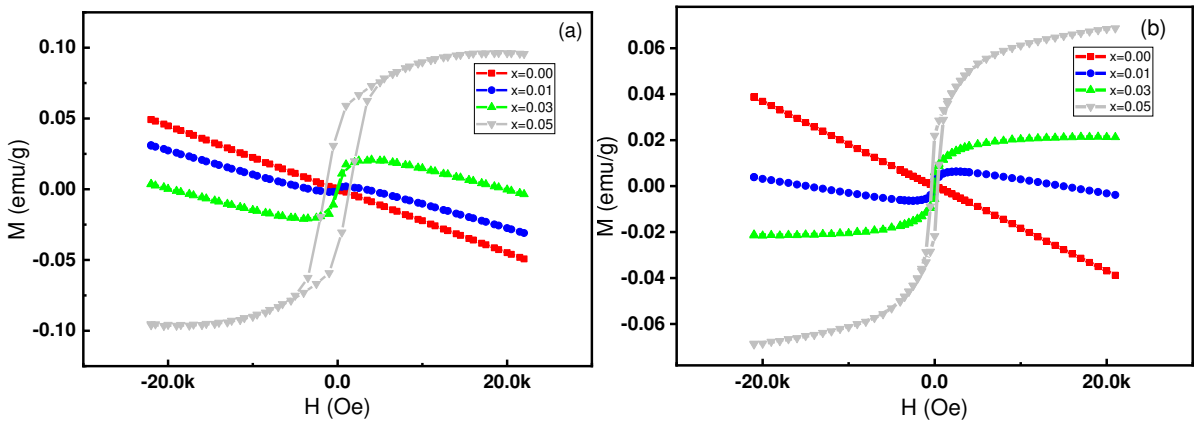

Figure 7. Magnetisation (M) vs. Magnetic Field (H) loops of (1-2x) KNN-xBFO-xBTO ceramics sintered by (a) CAS; (b) ConS

4. Conclusions

In this study, high-quality KNN-BTO-BFO ceramics were densified following a CAS procedure which consisted of cold sintering at 120°C followed by heat treatment (assisted sintering) for 4h at 1080°C. Their composition and microstructure were investigated carefully and the dielectric, piezoelectric and magnetic properties were measured. CAS samples were directly compared with ConS samples. CAS samples exhibited the highest values of relative density (>95%) which is attributed to a higher 'super-green' density generated through cold sintering at 120°C rather than dry pressing (ConS). The higher 'super-green' and final densities of CAS samples give rise to higher T_C and T_{O-T}, lower dielectric loss, and higher piezoelectric coefficients by $x \leq 0.01$, although coupling coefficients remained largely unaffected. The higher density also resulted in larger M and greater hysteresis in M-H measurements at equivalent compositions. Ultimately, CAS has the potential to assist in the production of high-performance KNN-based ceramics by addressing the issue of low sinterability in these materials by enhancing the densification at relatively low temperatures without sacrificing their properties.

Author Contributions: formal analysis, investigation, data curation, writing—original draft preparation, software, by HZ; conceptualization, supervision, methodology, validation, writing—review and editing, resources, by FH; project administration, co-supervision by AAS; data analysis tools, data curation help by SS; visualization, review by DW; and expert ideas, validation, and review by IMR.

Funding: This research received no external funding.

Acknowledgements: The authors of this research gratefully acknowledge the research support facilities of the Department of Materials Engineering, NED University of Engineering and Technology, and Sindh-HEC for lab facilities developed through funding (SHEC/SRSP/ET-2/19/2020-21).

Conflicts of Interest: The authors declare no conflict of interest.

References

1. Wang, D.; Hussain, F.; Khesro, A.; Feteira, A.; Tian, Y.; Zhao, Q.; Reaney, I.M. Composition and Temperature Dependence of Structure and Piezoelectricity in (1−x)(K1−yNay)NbO3-x(Bi1/2Na1/2)ZrO3 Lead-Free Ceramics. *J. Am. Ceram. Soc.* **2017**, *100*, 627–637, doi:10.1111/jace.14589.

2. Hussain, F.; Khesro, A.; Muhammad, R.; Wang, D. Effect of Ta-Doping on Functional Properties of K0.51Na0.49NbO3. *Mater. Res. Express* **2019**, *6*, 106309, doi:10.1088/2053-1591/AB3D49.

3. Wang, D.; Wang, G.; Lu, Z.; Al-Jlaihawi, Z.; Feteira, A. Crystal Structure, Phase Transitions and Photoferroelectric Properties of KNbO3-Based Lead-Free Ferroelectric Ceramics: A Brief Review. *Front. Mater.* **2020**, *7*, 91, doi:10.3389/FMATS.2020.00091/BIBTEX.

4. Hussain, F.; Khesro, A.; Lu, Z.; Wang, G.; Wang, D. Lead Free Multilayer Piezoelectric Actuators by Economically New Approach. *Front. Mater.* **2020**, *7*, 87, doi:10.3389/FMATS.2020.00087/BIBTEX.

5. Khesro, A.; Wang, D.; Hussain, F.; Muhammad, R.; Wang, G.; Feteira, A.; Reaney, I.M. Temperature Dependent Piezoelectric Properties of Lead-Free (1-x)K0.6Na0.4NbO3–XBiFeO3 Ceramics. *Front. Mater.* **2020**, *7*, 140, doi:10.3389/FMATS.2020.00140/BIBTEX.

6. Hussain, F.; Khesro, A.; Lu, Z.; Alotaibi, N.; Mohamad, A.A.; Wang, G.; Wang, D.; Zhou, D. Acceptor and Donor Dopants in Potassium Sodium Niobate Based Ceramics. *Front. Mater.* **2020**, *7*, 1–8, doi:10.3389/fmats.2020.00160.

7. Wu, J. Perovskite Lead-Free Piezoelectric Ceramics. *J. Appl. Phys.* **2020**, *127*, 190901, doi:10.1063/5.0006261.

8. Cong, L.; Huajing, W.; Jianzhang, M.; Baoyu, D.; Xiao, W.; Tengfei, L.; Xinghua, Z.; Xing, Y. Effect of Dwell Time on Cold Sintering Assisted Sintering Based Highly Transparent 0.9K0.5Na0.5NbO3-0.1LiBiO3 Ceramics. *J. Alloys Compd.* **2020**, *826*, 154249, doi:10.1016/j.jallcom.2020.154249.

9. Zhang, M.H.; Thong, H.C.; Lu, Y.X.; Sun, W.; Li, J.F.; Wang, K. (K,Na)NbO3-Based Lead-Free Piezoelectric Materials: An Encounter with Scanning Probe Microscopy. *J. Korean Ceram. Soc.* **2017**, *54*, 261–271, doi:10.4191/KCERS.2017.54.4.10.

10. Malič, B.; Koruza, J.; Hreščak, J.; Bernard, J.; Wang, K.; Fisher, J.G.; Benčan, A. Sintering of Lead-Free Piezoelectric Sodium Potassium Niobate Ceramics. *Materials (Basel).* **2015**, *8*, 8117–8146, doi:10.3390/MA8125449.

11. Li, J.F.; Wang, K.; Zhu, F.Y.; Cheng, L.Q.; Yao, F.Z. (K, Na) NbO3-Based Lead-Free Piezoceramics: Fundamental Aspects, Processing Technologies, and Remaining Challenges. **2013**, *96*, 3677–3696, doi:10.1111/JACE.12715.

12. Wang, D.; Siame, B.; Zhang, S.; Wang, G.; Ju, X.; Li, J.; Lu, Z.; Vardaxoglou, Y.; Whittow, W.; Cadman, D.; et al. Direct Integration of Cold Sintered, Temperature-Stable Bi2Mo2O9-K2MoO4 Ceramics on Printed Circuit Boards for Satellite Navigation Antennas. *J. Eur. Ceram. Soc.* **2020**, *40*, 4029–4034.

13. Funahashi, S.; Guo, J.; Guo, H.; Wang, K.; Baker, A.L.; Shiratsuyu, K.; Randall, C.A. Demonstration of the Cold Sintering Process Study for the Densification and Grain Growth of ZnO Ceramics. *J. Am. Ceram. Soc.* **2017**, *100*, 546–553, doi:10.1111/jace.14617.

14. Biesuz, M.; Sglavo, V.M. Beyond Flash Sintering: How the Flash Event Could Change Ceramics and Glass Processing. *Scr. Mater.* **2020**, *187*, 49–56, doi:10.1016/j.scriptamat.2020.05.065.

15. Liu, B.; Li, L.; Song, K.X.; Mao, M.M.; Lu, Z.; Wang, G.; Li, L.; Wang, D.; Zhou, D.; Feteira, A.; et al. Enhancement of Densification and Microwave Dielectric Properties in LiF Ceramics via a Cold Sintering and Post-Annealing Process. *J. Eur. Ceram. Soc.* **2021**, *41*, 1726–1729, doi:10.1016/j.jeurceramsoc.2020.09.073.

16. Goulas, A.; Chi-Tangyie, G.; Wang, D.; Zhang, S.; Ketharam, A.; Vaidhyanathan, B.; Reaney, I.M.; Cadman, D.A.; Whittow, W.G.; Vardaxoglou, J. (Yiannis) C.; et al. Additively Manufactured Ultra-Low Sintering Temperature, Low Loss Ag2Mo2O7 Ceramic Substrates. *J. Eur. Ceram. Soc.* **2021**, *41*, 394–401, doi:10.1016/j.jeurceramsoc.2020.08.031.

17. Ji, Y.; Song, K.; Zhang, S.; Lu, Z.; Wang, G.; Li, L.; Zhou, D.; Wang, D.; Reaney, I.M. Cold Sintered, Temperature-Stable CaSnSiO5-K2MoO4 Composite Microwave Ceramics and Its Prototype Microstrip Patch Antenna. *J. Eur. Ceram. Soc.* **2021**, *41*, 424–429.

18. Goulas, A.; Chi-Tangyie, G.; Wang, D.; Zhang, S.; Ketharam, A.; Vaidhyanathan, B.; Reaney, I.M.; Cadman, D.A.; Whittow, W.G.; Vardaxoglou, J. (Yiannis) C.Y.C.; et al. Microstructure and Microwave Dielectric Properties of 3D Printed Low Loss Bi2Mo2O9 Ceramics for LTCC Applications. *Appl. Mater. Today* **2020**, *21*, doi:10.1016/j.apmt.2020.100862.

19. Lu, Z.; Bao, W.; Wang, G.; Sun, S.K.; Li, L.; Li, J.; Yang, H.; Ji, H.; Feteira, A.; Li, D.; et al. Mechanism of Enhanced Energy Storage Density in AgNbO3-Based Lead-Free Antiferroelectrics. *Nano Energy* **2021**, *79*, doi:10.1016/j.nanoen.2020.105423.

20. Wu, F.F.; Zhou, D.; Xia, S.; Zhang, L.; Qiao, F.; Pang, L.X.; Sun, S.K.; Zhou, T.; Singh, C.; Sombra,

A.S.B.; et al. Low Sintering Temperature, Temperature-Stable Scheelite Structured Bi[V1−x (Fe1/3W 2/3)x]O4 Microwave Dielectric Ceramics. *J. Eur. Ceram. Soc.* **2022**, *42*, 5731–5737, doi:10.1016/J.JEURCERAMSOC.2022.05.036.

21. Serrazina, R.; Gomes, M.; Vilarinho, R.; Pereira, L.; Dean, J.S.; Reaney, I.M.; Senos, A.M.O.R.; Vilarinho, P.M.; Moreira, J.A. Induced Internal Stresses and Their Relation to FLASH Sintering of KNN Ceramics. *J. Mater. Chem. C* **2022**, doi:10.1039/D2TC01680J.

22. Serrazina, R.; Dean, J.S.; Reaney, I.M.; Pereira, L.; Vilarinho, P.M.; Senos, A.M.O.R. Mechanism of Densification in Low-Temperature FLASH Sintered Lead Free Potassium Sodium Niobate (KNN) Piezoelectrics. *J. Mater. Chem. C* **2019**, *7*, 14334–14341, doi:10.1039/C9TC03117K.

23. Yu, M.; Grasso, S.; Mckinnon, R.; Saunders, T.; Reece, M.J. Review of Flash Sintering: Materials, Mechanisms and Modelling. *Adv. Appl. Ceram.* **2017**, *116*, 24–60.

24. Wang, D.; Zhou, D.; Zhang, S.; Vardaxoglou, Y.; Whittow, W.G.; Cadman, D.; Reaney, I.M. Cold-Sintered Temperature Stable Na0.5Bi0.5MoO4-Li2MoO4 Microwave Composite Ceramics. *ACS Sustain. Chem. Eng.* **2018**, *6*, 2438–2444, doi:10.1021/acssuschemeng.7b03889.

25. Ji, Y.; Song, K.; Luo, X.; Liu, B.; Barzegar Bafrooei, H.; Wang, D. Microwave Dielectric Properties of (1-x) Li2MoO4–XMg2SiO4 Composite Ceramics Fabricated by Cold Sintering Process. *Front. Mater.* **2019**, *6*, doi:10.3389/FMATS.2019.00256/FULL.

26. Wang, D.; Zhang, S.; Wang, G.; Vardaxoglou, Y.; Whittow, W.; Cadman, D.; Zhou, D.; Song, K.; Reaney, I.M. Cold Sintered CaTiO3-K2MoO4 Microwave Dielectric Ceramics for Integrated Microstrip Patch Antennas. *Appl. Mater. Today* **2020**, *18*, doi:10.1016/j.apmt.2019.100519.

27. Wang, D.; Chen, J.; Wang, G.; Lu, Z.; Sun, S.; Li, J.; Jiang, J.; Zhou, D.; Song, K.; Reaney, I.M. Cold Sintered LiMgPO4 Based Composites for Low Temperature Co-Fired Ceramic (LTCC) Applications. *J. Am. Ceram. Soc.* **2020**, *103*, 6237–6244, doi:10.1111/JACE.17320.

28. Wang, D.; Zhou, D.; Song, K.; Feteira, A.; Randall, C.A.; Reaney, I.M. Cold-Sintered C0G Multilayer Ceramic Capacitors. *Adv. Electron. Mater.* **2019**, *5*, 1900025, doi:10.1002/AELM.201900025.

29. Ma, M.; Song, K.; Ji, Y.; Hussain, F.; Khesro, A.; Mao, M.; Xue, L.; Xu, P.; Liu, B.; Lu, Z.; et al. 5G Microstrip Patch Antenna and Microwave Dielectric Properties of Cold Sintered LiWVO6–K2MoO4 Composite Ceramics. *undefined* **2021**, *47*, 19241–19246, doi:10.1016/J.CERAMINT.2021.03.179.

30. Wang, D.; Li, L.; Jiang, J.; Lu, Z.; Wang, G.; Song, K.; Zhou, D.; Reaney, I.M. Cold Sintering of Microwave Dielectric Ceramics and Devices. *J. Mater. Res. 2021 362* **2021**, *36*, 333–349, doi:10.1557/S43578-020-00029-W.

31. Deng, B.; Ma, Y.; Chen, T.; Wang, H.; Lin, J.; Lin, C.; Wu, X.; Zhao, C.; Lin, T.; Gao, M.; et al. Elevating Electrical Properties of (K, Na)NbO3 Ceramics via Cold Sintering Process and Post-Annealing. *J. Am. Ceram. Soc.* **2022**, *105*, 461–468, doi:10.1111/jace.18103.

32. Tsuji, K.; Fan, Z.; Bang, S.H.; Dursun, S.; Trolier-McKinstry, S.; Randall, C.A. Cold Sintering of the Ceramic Potassium Sodium Niobate, (K0.5Na0.5)NbO3, and Influences on Piezoelectric Properties. *J. Eur. Ceram. Soc.* **2022**, *42*, 105–111, doi:10.1016/j.jeurceramsoc.2021.10.002.

33. Yu, T.; Cheng, J.; Li, L.; Sun, B.; Bao, X.; Zhang, H. Current Understanding and Applications of the Cold Sintering Process. *Front. Chem. Sci. Eng.* **2019**, *13*, 654–664, doi:10.1007/s11705-019-1832-1.

34. Nelo, M.; Peräntie, J.; Siponkoski, T.; Juuti, J.; Jantunen, H. Upside-down Composites: Electroceramics without Sintering. *Appl. Mater. Today* **2019**, *15*, 83–86, doi:10.1016/j.apmt.2018.12.021.

35. Liu, M.; Jin, Q.; Shen, P. Cold Sintering of NaNO3/MgO Heat-Storage Composite. *Ceram. Int.* **2020**, *46*, 28955–28960, doi:10.1016/j.ceramint.2020.08.066.

36. Guo, H.; Guo, J.; Baker, A.; Randall, C.A. Hydrothermal-Assisted Cold Sintering Process: A New

Guidance for Low-Temperature Ceramic Sintering. *ACS Appl. Mater. Interfaces* **2016**, *8*, 20909–20915, doi:10.1021/ACSAMI.6B07481/SUPPL_FILE/AM6B07481_SI_001.PDF.

37. Santha, N.; Rakhi, M.; Subodh, G. Fabrication of High Quality Factor Cold Sintered MgTiO3–NaCl Microwave Ceramic Composites. *Mater. Chem. Phys.* **2020**, *255*, 123636, doi:10.1016/j.matchemphys.2020.123636.

38. Guo, J.; Guo, H.; Baker, A.L.; Lanagan, M.T.; Kupp, E.R.; Messing, G.L.; Randall, C.A. Cold Sintering: A Paradigm Shift for Processing and Integration of Ceramics. *Angew. Chemie - Int. Ed.* **2016**, *55*, 11457–11461, doi:10.1002/anie.201605443.

39. Induja, I.J.; Sebastian, M.T. Microwave Dielectric Properties of Cold Sintered Al2O3-NaCl Composite. *Mater. Lett.* **2018**, *211*, 55–57, doi:10.1016/j.matlet.2017.09.083.

40. Ma, J.P.; Chen, X.M.; Ouyang, W.Q.; Wang, J.; Li, H.; Fang, J.L. Microstructure, Dielectric, and Energy Storage Properties of BaTiO3 Ceramics Prepared via Cold Sintering. *Ceram. Int.* **2018**, *44*, 4436–4441, doi:10.1016/j.ceramint.2017.12.044.

41. Cao, W.; Li, T.; Chen, P.; Wang, C. Outstanding Energy Storage Performance of Na0.5Bi0.5TiO3-BaTiO3-(Sr0.85Bi0.1)(Mg1/3Nb2/3)O3Lead-Free Ceramics. *ACS Appl. Energy Mater.* **2021**, *4*, doi:10.1021/acsaem.1c01566.

42. Wang, T.; Liu, J.; Kong, L.; Yang, H.; Wang, F.; Li, C. Evolution of the Structure, Dielectric and Ferroelectric Properties of Na0.5Bi0.5TiO3-Added BaTiO3–Bi(Mg2/3Nb1/3)O3 Ceramics. *Ceram. Int.* **2020**, *46*, doi:10.1016/j.ceramint.2020.07.007.

43. Nuraini, U.; Triyuliana, N.A.; Mashuri, M.; Suasmoro, S. Characterization of Relaxor Ferroelectrics from BiFeO3 Doped (K0.5Na0.5)NbO3 Systems. *IOP Conf. Ser. Mater. Sci. Eng.* **2019**, *496*, 0–6, doi:10.1088/1757-899X/496/1/012043.

44. Structure Database Dissolution Precipitation. **2005**.

45. Ma, J.; Li, H.; Wang, H.; Lin, C.; Wu, X.; Lin, T.; Zheng, X.; Yu, X. Composition, Microstructure and Electrical Properties of K0.5Na0.5NbO3 Ceramics Fabricated by Cold Sintering Assisted Sintering. *J. Eur. Ceram. Soc.* **2019**, *39*, 986–993, doi:10.1016/j.jeurceramsoc.2018.11.044.

46. Beltrami, R.; Mercadelli, E.; Baldisserri, C.; Galassi, C.; Braghin, F.; Lecis, N. Synthesis of KNN Powders: Scaling Effect of the Milling Step. *Powder Technol.* **2020**, *375*, 101–108, doi:10.1016/j.powtec.2020.07.098.

47. Wu, J.; Zhao, G.; Pan, C.; Tong, P.; Yang, J.; Zhu, X.; Yin, L.; Song, W.; Sun, Y. Simultaneously Enhanced Piezoelectricity and Curie Temperature in BiFeO3-Based High Temperature Piezoelectrics. *J. Eur. Ceram. Soc.* **2021**, *41*, 7645–7653, doi:10.1016/j.jeurceramsoc.2021.08.030.

48. Hussain, F.; Sterianou, I.; Khesro, A.; Sinclair, D.C.; Reaney, I.M. P-Type/n-Type Behaviour and Functional Properties of KxNa(1-x)NbO3 ($0.49 \leq x \leq 0.51$) Sintered in Air and N2. *J. Eur. Ceram. Soc.* **2018**, *38*, 3118–3126, doi:10.1016/j.jeurceramsoc.2018.03.013.

49. Shirane, G.; Newnham, R.; Pepinsky, R. Dielectric Properties and Phase Transitions of NaNbO3 and (Na,K)NbO3. *Phys. Rev.* **1954**, *96*, 581–588, doi:10.1103/PHYSREV.96.581.

50. Zhen, Y.; Li, J.F. Normal Sintering of (K,Na)NbO3-Based Ceramics: Influence of Sintering Temperature on Densification, Microstructure, and Electrical Properties. *J. Am. Ceram. Soc.* **2006**, *89*, 3669–3675, doi:10.1111/J.1551-2916.2006.01313.X.

51. Guo, J.; Floyd, R.; Lowum, S.; Maria, J.P.; Herisson De Beauvoir, T.; Seo, J.H.; Randall, C.A. Cold Sintering: Progress, Challenges, and Future Opportunities. *Annu. Rev. Mater. Res.* **2019**, *49*, 275–295, doi:10.1146/annurev-matsci-070218-010041.

52. Xu, K.; Li, J.; Lv, X.; Wu, J.; Zhang, X.; Xiao, D.; Zhu, J. Superior Piezoelectric Properties in Potassium–Sodium Niobate Lead-Free Ceramics. *Adv. Mater.* **2016**, *28*, 8519–8523, doi:10.1002/ADMA.201601859.

53. Moriana, A.D.; Zhang, S. Lead-Free Textured Piezoceramics Using Tape Casting: A Review. *J. Mater.* **2018**, *4*, 277–303, doi:10.1016/J.JMAT.2018.09.006.

54. Ghosh, A.; Trujillo, D.P.; Choi, H.; Nakhmanson, S.M.; Alpay, S.P.; Zhu, J.X. Electronic and Magnetic Properties of Lanthanum and Strontium Doped Bismuth Ferrite: A First-Principles Study. *Sci. Reports 2019 91* **2019**, *9*, 1–10, doi:10.1038/s41598-018-37339-3.

55. Liu, Q.; Liu, J.; Lu, D.; Li, T.; Zheng, W. Dense Sm and Mn Co-Doped BaTiO3 Ceramics with High Permittivity. *Materials (Basel).* **2019**, *12*, doi:10.3390/MA12040678.

56. Politova, E.D.; Kaleva, G.M.; Mosunov, A. V.; Sadovskaya, N. V.; Kiselev, D.A.; Kislyuk, A.M.; Ilina, T.S.; Yu. Stefanovich, S.; Fortalnova, E.A. Structure, Ferroelectric and Local Piezoelectric Properties of KNN-Based Perovskite Ceramics. *Ferroelectrics* **2020**, *560*, 38–47, doi:10.1080/00150193.2020.1722881.

57. Yang, S.; Dong, G.; Guan, R.; Wu, D. Effect of KNN Doping on the Dielectric Properties of BaTiO3 Lead-Free Ceramics. *J. Mater. Sci. Mater. Electron.* **2022**, *33*, 810–816, doi:10.1007/S10854-021-07351-X/FIGURES/8.

58. Zhang, Y.; Li, M.; Yang, S.; Zhai, J. Low-Temperature Sintering of KNN-Based Lead Free Ceramics. *Solid State Commun.* **2021**, *324*, 114133, doi:10.1016/J.SSC.2020.114133.

59. Dai, Z.; Zhang, F.; Rafiq, M.N.; Liu, C.; Wang, X.; Gu, S.; Yasui, S. Design of a KNN-BZT Ceramic with High Energy Storage Properties and Transmittance under Low Electric Fields. *ACS Omega* **2023**, *8*, 7883–7890, doi:10.1021/ACSOMEGA.2C07646/ASSET/IMAGES/LARGE/AO2C07646_0008.JPEG.

60. Bharathi, P.; Varma, K.B.R. Effect of the Addition of B2O3 on the Density, Microstructure, Dielectric, Piezoelectric and Ferroelectric Properties of K 0.5Na0.5NbO3 Ceramics. *J. Electron. Mater.* **2014**, *43*, 493–505, doi:10.1007/S11664-013-2939-7.

61. Andrews, J.; Button, D.; Reaney, I.M. Improving Energy Consumption and Unlocking New Potential in Component Manufacturing. *Johnson Matthey Technol. Rev.* **2020**, *64*, 219–232, doi:10.1595/205651320X15814150061554.

62. Won, S.S.; Kawahara, M.; Glinsek, S.; Lee, J.; Kim, Y.; Jeong, C.K.; Kingon, A.I.; Kim, S.H. Flexible Vibrational Energy Harvesting Devices Using Strain-Engineered Perovskite Piezoelectric Thin Films. *Nano Energy* **2019**, *55*, 182–192, doi:10.1016/J.NANOEN.2018.10.068.

63. Nuraini, U.; Triyuliana, N.A.; Mashuri, M.; Kidkhunthod, P.; Suasmoro, S. Local Distortion Determination of the (1 − x) (K0.5Na0.5)NbO3 − x (Ba0.8Sr0.2)TiO3 System and Their Influence on the Electrical Properties. *J. Mater. Sci. Mater. Electron.* **2018**, *29*, 1139–1145, doi:10.1007/s10854-017-8016-x.

64. Vendrell, X.; García, J.E.; Bril, X.; Ochoa, D.A.; Mestres, L.; Dezanneau, G. Improving the Functional Properties of (K0.5Na0.5)NbO3 Piezoceramics by Acceptor Doping. *J. Eur. Ceram. Soc.* **2015**, *35*, 125–130, doi:10.1016/j.jeurceramsoc.2014.08.033.

65. Hao, J.; Li, W.; Zhai, J.; Chen, H. Progress in High-Strain Perovskite Piezoelectric Ceramics. *Mater. Sci. Eng. R Reports* **2019**, *135*, 1–57, doi:10.1016/J.MSER.2018.08.001.

66. Rubio-Marcos, F.; Ochoa, P.; Fernandez, J.F. Sintering and Properties of Lead-Free (K,Na,Li)(Nb,Ta,Sb)O3 Ceramics. *J. Eur. Ceram. Soc.* **2007**, *27*, 4125–4129, doi:10.1016/J.JEURCERAMSOC.2007.02.110.

67. Yao, F.Z.; Wang, K.; Cheng, L.Q.; Zhang, X.; Zhang, W.; Zhu, F.; Li, J.F. Nanodomain Engineered (K, Na)NbO3 Lead-Free Piezoceramics: Enhanced Thermal and Cycling Reliabilities. *J. Am. Ceram. Soc.* **2015**, *98*, 448–454, doi:10.1111/JACE.13265.

68. Men, T.L.; Thong, H.C.; Li, J.T.; Li, M.; Zhang, J.; Zhong, V.; Luo, J.; Chu, X.; Wang, K.; Li, J.F. Domain Growth Dynamics in (K, Na)NbO3 Ferroelectric Thin Films. *Ceram. Int.* **2017**, *43*, 9538–9542, doi:10.1016/J.CERAMINT.2017.03.180.

69. Wang, K.; Yao, F.Z.; Jo, W.; Gobeljic, D.; Shvartsman, V. V.; Lupascu, D.C.; Li, J.F.; Rödel, J. Temperature-Insensitive (K,Na)NbO3-Based Lead-Free Piezoactuator Ceramics. *Adv. Funct. Mater.* **2013**, *23*, 4079–4086, doi:10.1002/ADFM.201203754.

70. França, E.L.T.; Romanholo, P.V.V.; Simões, S.S.; Falcão, E.H.L.; Franco, A.; Machado, F.L.A. Enhancing the Electrical Properties of NBT Ceramics by the Addition of Small Amounts of Yb. *J. Alloys Compd.* **2021**, *873*, doi:10.1016/j.jallcom.2021.159845.

71. Lin, Y.; Liu, X.; Yang, H.; Wang, F.; Liu, C. Low Temperature Sintering of Laminated Ni0.5Ti0.5NbO4-Ni0.8Zn0.2Fe2O4 Composites for High Frequency Applications. *Ceram. Int.* **2016**, *42*, 11265–11269, doi:10.1016/j.ceramint.2016.04.042.

72. Guo, J.; Legum, B.; Anasori, B.; Wang, K.; Lelyukh, P.; Gogotsi, Y.; Randall, C.A. Cold Sintered Ceramic Nanocomposites of 2D MXene and Zinc Oxide. *Adv. Mater.* **2018**, *30*, 1–6, doi:10.1002/adma.201801846.

73. Chen, N.; Xiao, B.; Xu, X.; Sun, T.; Chen, M.; Hu, R.; Deng, X.; Chen, X.; Wang, H. Cold-Sintered Ni0.2Cu0.2Zn0.6Fe2O4-Li2MoO4 Ceramic Composites with Enhanced Magnetodielectric Properties. *J. Eur. Ceram. Soc.* **2021**, *41*, 1310–1316, doi:10.1016/j.jeurceramsoc.2020.09.034.

74. Elayaperumal, E.; Murugesan, G.; Malathi, M. Observation of Magnetoelectric Effect in CuO-Doped SrBi4Ti4O15 Ceramics. *Mater. Lett.* **2021**, *300*, doi:10.1016/J.MATLET.2021.130048.

75. Jabeen, N.; Rehman, A.U.; Hassan, N.U.; Qaiser, M.A.; Zaidi, A.; Khan, M.U.; Khan, I.A.; Nouman, M. Boosting of Magnetic, Ferroelectric, Energy Storage Efficiency, and Piezoelectric Properties of Zn Intercalated SrBi4Ti4O15-Based Ceramics. *Mater. (Basel, Switzerland)* **2022**, *15*, doi:10.3390/MA15145057.